



Microstructure, mechanical properties and corrosion behavior of austenitic stainless steel sheet joints welded by gas tungsten arc (GTA) and ultrasonic–wave–assisted gas tungsten pulsed arc (U–GTPA)

Weifeng Xie^{1,2} · Chunli Yang²

Received: 21 December 2019 / Revised: 20 February 2020 / Accepted: 20 March 2020 / Published online: 2 April 2020
© Wrocław University of Science and Technology 2020

Abstract

Here, ultrasonic–wave–assisted gas tungsten pulsed arc (U–GTPA) welding is proposed as a new alternative welding process to gas tungsten arc (GTA) welding. To better understand the advantages of this new process, in this paper, the microstructure, mechanical properties and corrosion behavior of GTA- and U–GTPA-welded joints of 316L stainless steel are systematically compared. These results show that the weld zone (WZ) depth-to-width ratio of the U–GTPA-welded joint increased, and the area of the equiaxed grain zone was larger than that of the GTA-welded joint. This results in finally increasing the strength and hardness for U–GTPA-welded joints, and the ultimate tensile strength and elongation of the U–GTPA-welded joints were 7.1% and 26.2% greater than those of the GTA-welded joint, respectively. For the U–GTPA-welded joint, under the action of the pulsed arc, the grain distribution with high-angle boundaries (HABs) was different from that of the GTA-welded joint. The minimum of the HAB fraction corresponded to the fracture position for both joints in tensile tests. It shows that a large number of HABs were beneficial in improving joint tensile properties. However, for electrochemical corrosion experiments of two WZs in 3.5% NaCl solution, despite this GTA WZ having a higher HAB fraction, the corrosion current density and corrosion potential of U–GTA WZ were lower and higher than those of the GTA WZ, respectively. The corrosion rate and corrosion sensitivity of U–GTPA WZ indicated good corrosion resistance.

Keywords Austenitic stainless steel · GTA welding · U–GTPA welding · Microstructure · Mechanical properties · Corrosion behavior

1 Introduction

Austenitic stainless steel is a series of stainless steels that have a matrix structure of mainly austenite, which is obtained by adding austenite-forming elements, such as Ni, Mo, N, Cu and Mn into stainless steel matrix with a Cr content of 17–20% and relatively less amount of carbon [1, 2]. Compared with other stainless steels, austenitic

stainless steel has excellent ductility, formability, toughness and corrosion resistance, and their excellent properties are also attributed to the presence of high concentration of these elements [3, 4]. In the stainless–steel family, austenitic stainless steel is the most widely used, accounting for approximately two-thirds of total output and is widely used in aerospace [5], energy [6] and transportation [7], as well as in chemical industry [8]. One type of austenitic stainless steels, 316L, is often used in pipes for sea water heat pump systems. This material is exposed to sea water in practical applications, and there is variation in the conductivity of sea water, which inevitably affects the electrochemical resistance of the steel. However, welded joints of 316L stainless steel are prone to thermal cracking, intergranular corrosion and embrittlement [7, 9]. More generally, due to the existence of welding defects, the dramatic change in welding stress and the decline in the mechanical properties of the welded joint, all of these factors can cause welded joints to become a weak link in the overall welding system. The

Electronic supplementary material The online version of this article (<https://doi.org/10.1007/s43452-020-00044-y>) contains supplementary material, which is available to authorized users.

✉ Weifeng Xie
xiewf1985@163.com

¹ School of Mechanical Engineering, Northeast Electric Power University, Jilin 132012, China

² State Key Laboratory of Advanced Welding and Joining, Harbin Institute of Technology, Harbin 150001, China

main reason is the difference between the metallographic structure of the weld and the base metal (BM) due to different processing techniques, so welding researchers have been paying more attention to the welding process and methods to improve the structure and properties of the joints.

Fusion welding is the most widely used method of welding in various industrial fields owing to its mature technology, simple operation, easy automation and other advantages. Gao et al. [10] comparatively studied the butt welding of 316L stainless steel plate with a thickness of 5.5 mm by laser–gas metal arc (GMA) and laser welding and found that microstructures in the laser–GMA weld zone (WZ) mainly consisted of columnar and equiaxed dendrites, while only columnar dendrites could be observed in the laser WZ. The ratio of temperature gradient to cooling rate in WZ center influenced by laser and arc was considered smaller than that of keyhole zone center; therefore, more equiaxed dendrites existed. Feng et al. [11] found that the WZ was comprised of austenite and δ -ferrite phases in a keyhole gas tungsten arc (GTA)-welded 316L stainless steel plate. The formation of δ -ferrite in the WZ was the consequence of higher heat input during welding. Garcia et al. [12] studied the corrosion behavior of GMA-welded 316L stainless steel joints by the electrochemical test and also revealed that the heat-affected zone (HAZ) was more prone to pitting corrosion owing to the higher heat input. Tseng et al. [13] investigated the effect of activated GTA welding process with five kinds oxide fluxes on weld morphology and hardness of 316L stainless steels. This result suggested that GTA welding with SiO_2 and MoO_3 fluxes achieved an increase in weld depth and a decrease in bead width, respectively, but the addition of oxide flux did not significantly affect the hardness of 316L stainless steel-activated GTA WZ. Sabzi et al. [14] reported the influence of applying electromagnetic vibration during GTA welding on the microstructural transformations and mechanical properties in 316L stainless steel welding joints and observed that increasing the intensity of electromagnetic vibration resulted in the intense reduction in dendrite sizes in WZ and finally increasing the strength and hardness.

In recent years, in view of the features of ultrasonic processes [15, 16] and to further improve the quality and efficiency of welding [17], the combination of ultrasonic and arc welding has drawn the interest of welding researchers. In arc welding, the most direct way to apply ultrasound is to rigidly fix an ultrasonic generator to the workpiece to be welded together and use ultrasonic vibrations to affect the solidification process of the weld pool. Han et al. [18] found that after applying ultrasonic vibrations at a frequency of 20 kHz, the micro-mixing zone in the WZ markedly decreased; some areas disappeared, and the corrosion resistance of the WZ improved in the manual arc welding of super-austenitic stainless steel. Sun et al. [19] proposed

ultrasonic–wave–assisted GTA (U–GTA) welding in which ultrasound was emitted through an ultrasonic radiator on the same axis as the arc and the ultrasonic field acted on the arc and the weld pool at the same time. Since the ultrasonic vibration was not directly applied to the workpiece to be welded, no more rigid fixation was required. In welding tests of 304 stainless steel, the arc pressure increased, the weld grain refined, and the strength of the welded joint increased by 8%. This welding system has the advantages of a simple implementation, no limitations on the welding position and is suitable for use with both non–melting and melting electrodes. In further research, Xie et al. [20] confirmed that by optimizing the shape and geometric size of the ultrasonic radiator of the U–GTA welding gun, the ultrasonic field strength was markedly improved, and the energy loss caused by acoustic scattering also decreased. Under conditions of a concave spherical ultrasonic radiator, the directional acoustic pressure acting on the arc from the outside to the inside reached a maximum, and the effect of acoustic restraint was the strongest. In direct current (DC) GTA welding, a kind of pulsed arc plasma with restraint was found, as shown in Fig. 1 (or see Supplemental Video 1 for conventional arc and Supplemental Video 2 for pulsed arc). Unlike the conventional divergent arc, in which the arc plasma was compressed by ultrasound, there was a high bright agglomeration zone in the arc, which vibrated periodically at a certain frequency [21]. Notably, the U–GTPA is unlike the original U–GTA. The latter uses a plane ultrasonic radiator, which tends to dissipate ultrasonic energy. The directivity of the ultrasonic pressure (acoustic focusing effect) on the arc is very weak and the area of effect is very small. Only the arc boundary compression appears in the macro-view and the arc is not controllable. This pulsed arc is also different from a DC pulsed GTA. The arc of the latter system is controlled by the pulse current of the welding power supply through a relatively complex mechanism, and there are more adjustable welding specification parameters.

Since the discovery of U–GTPA, there has been little research on this welding process and its effectiveness in practical welding applications remains unclear. In this paper, the pulsed arc welding process is termed ultrasonic–wave–assisted tungsten pulsed arc (U–GTPA) welding. The influence of the pulsed arc thermal distribution on the weld appearance, microstructure, mechanical properties and corrosion resistance is systematically analyzed by this comparative study of GTA- and U–GTPA-welded joints of 316L stainless steel. The mechanisms leading to a range of joint performance varieties are revealed. This study will further help to optimize the arc heat source and promote applications of the pulsed arc welding in precision and efficient welding–based manufacturing.

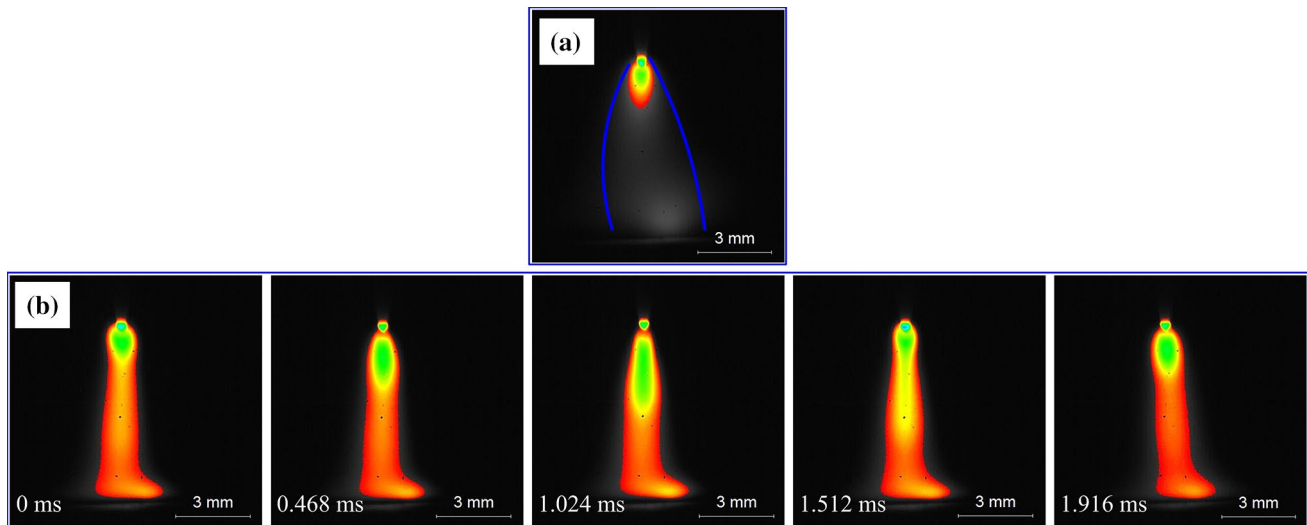


Fig. 1 The shapes for **a** conventional arc and **b** pulsed arc [21]

2 Experimental procedure

2.1 Materials

A 2.0-mm-thick 316L stainless steel sheet was selected as the BM, the 316L stainless steel sheet was cold-rolled plate, and its chemical composition is shown in Table 1. In this study, all the welding tests were flat butt-welded without filler wire. The size of all the parts to be welded was 300.0 mm × 100.0 mm. Before welding, we observed the surface of the sheet to be welded, which was flat and free of scratches, dents and other defects. If these requirements were not met, the welding surface was polished successively with sand paper 180 and 360#, while ensuring parallelism of the welding surface. The welding surface was thoroughly wiped with alcohol. Oil stains within 20 mm of the welding zone also were cleaned. After wiping, the welding processes were performed after the alcohol completely volatilized. During the welding process, the 316L stainless steel sheet to be welded was pressed by the welding fixture to ensure that the two sheets were spliced in parallel and the gap between them was set to 0.5 mm.

2.2 U-GTPA welding

For GTA and U-GTPA welding, all sheets were welded by a U-GTPA welding setup and the schematic of the setup is shown in Fig. 2. During welding, only the workpiece moved by setting a constant welding speed, while the welding gun

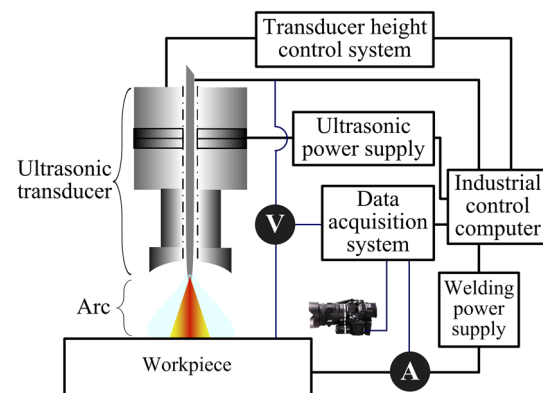


Fig. 2 Schematic diagram of U-GTPA welding setup

was fixed above the workpiece, the axis of the welding gun was guaranteed to be perpendicular to the workpiece along the welding direction. This setup mainly included two parts: a welding system and an ultrasonic radiation system, the former produced a welding arc and the later generated ultrasonic waves. The ultrasonic radiation system consisted of the ultrasonic power supply and ultrasonic transducer. The synchronized mechanical vibration was generated by the transducer and radiated into space through the ultrasonic radiator in the form of ultrasonic waves. The ultrasonic field acted on the arc and the weld pool at the same time.

Table 1 Chemical composition of 316L stainless steel

| Elements | C | Cr | Ni | Mn | Mo | Si | Co | N | P | S | Fe |
|----------|------|-------|-------|------|------|------|------|------|------|------|-----|
| Wt% | 0.03 | 18.66 | 10.02 | 1.65 | 2.05 | 0.37 | 0.21 | 0.02 | 0.03 | 0.01 | Bal |

The ultrasonic excitation frequency was 20 kHz. According to the results reported by Xie et al. [20], a concave spherical surface was selected as the shape of the ultrasonic radiator and the detailed shape parameters are listed in Fig. 3. For the U–GTPA welding, the SY–2000 ultrasonic power supply was used and its input power was limited to 2000 W. When the power was turned off, GTA welding was performed normally without ultrasonic. All welding parameters were the same in both welding processes. A TransTig 2500 welding power supply was applied in our study, and all welding tests were conducted under direct current electrode negative conditions. The diameter of the tungsten electrode was 3.2 mm. Commercially available argon of 99.99% purity was used as the shielding gas, and the airflow was set to 15 L/min. Welding tests were carried out at a welding speed, welding current and arc height of 2.5 mm/min, 100 A and 4 mm, respectively. The pulsation frequency of the arc was 570 Hz.

2.3 Microstructural characterization

Before evaluating the microstructure characterization for both joints, metallographic specimens need to be carefully prepared. In our study, metallographic samples were cut out from the welded joint by a wire electrical discharge machine, mounted, mechanically polished and subsequently etched for approximately 5 s at room temperature with a solution containing 50 mL HNO_3 , 100 mL HCl , 1 mL HF and 10 g CuSO_4 . Macro-images of joint sections were examined with the use of a SZX12 stereoscopic microscope. Then, the microstructures of the WZ, HAZ and BM were obtained by a GX71 optical microscope. Additionally, the grain morphologies for those typical regions were also obtained by a Nova 400 field emission scanning electron microscope,

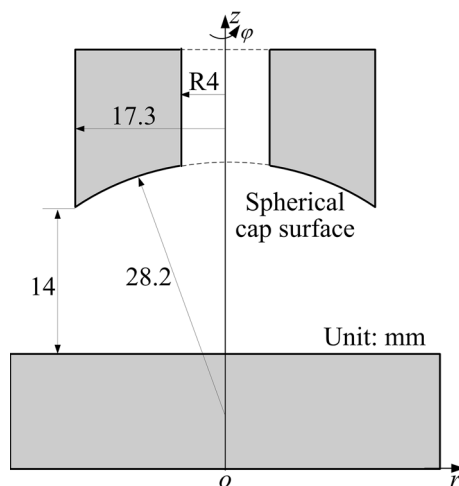


Fig. 3 Shape parameters for the ultrasonic radiator in U–GTPA welding gun

which was mainly used for the analysis of electron backscatter diffraction (EBSD), while HKL Channel 5 software was used to collect the diffraction data. Samples for EBSD were prepared by traditional mechanical polishing followed by electropolishing at 20 °C with a 98 vol.% ethyl alcohol and 2 vol.% perchloric acid solution applying 45 V for 20 s. At this stage, a TD–3500 X–ray diffraction (XRD) instrument was applied for the analysis of phase structure in BM and WZs of both joints.

2.4 Mechanical properties

The mechanical properties for both joints were evaluated by microhardness and tensile testing. A DMH–2LS microhardness tester was applied to obtain the joint Vickers hardness along the center line in the thickness direction comprising three typical regions. The load was 300 gf, the dwell time was 15 s, and the interval between two points was 0.2 mm. All tensile specimens were machined to the required dimensions as shown in Fig. 4, by a wire electrical discharge machine. All tensile tests were performed at the ambient temperature of the BM and the joints in accordance with GB/T 228.1–2010 standard for metal tensile testing [22], on an Instron 5569 tensile testing machine. The strain rate was 1/s, the gauge length was 25 mm, and each final tensile result was the mean value of three tests.

2.5 Electrochemical corrosion

Electrochemical tests were carried out on a CHI660E electrochemistry workstation by a three–electrode system. A platinum flake and a saturated calomel electrode (SCE) with a Luggin capillary were used as the auxiliary and reference electrode, respectively. At the same time, a metal flake of $2.0 \times 2.0 \times 15.0 \text{ mm}^3$ from the BM and WZs in both joints were used as the working electrodes, and the surface area

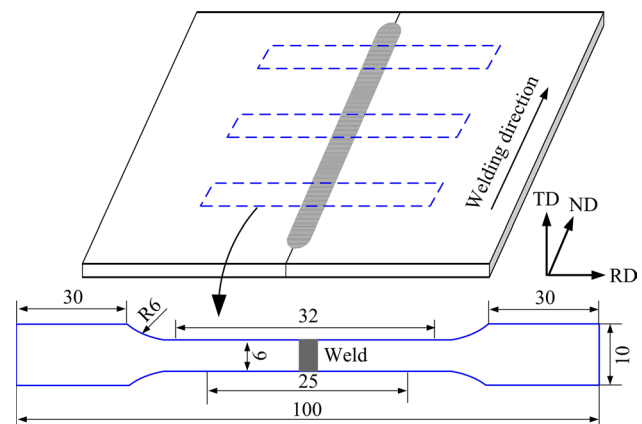


Fig. 4 Dimensions of tensile specimens (unit: mm)

of effective working electrode was 20.0 mm^2 . All working electrodes were ground with SiC emery papers of up to 2000 grit, finely polished with $1.5 \mu\text{m}$ diamond powder, then rinsed with ethanol for 30 s and dried in air. All non-tested surfaces were coated using a stop-off gelatin. The potentiodynamic polarization tests were conducted at potentials ranging from -0.1 to $1.0 V_{\text{SCE}}$ in a 3.5 wt% NaCl solution ($\text{pH}=6$) at the scan rate of 0.5 mV/s and $25 \pm 1 \text{ }^\circ\text{C}$ after all samples were immersed in the same solution for 30 min. Additionally, 1200-s potentiostatic polarization tests at the polarization potential of $0.5 V_{\text{SCE}}$ were performed to understand the corrosion mechanism. Each electrochemical test was performed three times, and the final result was also an average. The corroded specimens were then carefully examined by a Quanta 200FEG scanning electron microscope (SEM) with an energy-dispersive x-ray spectrometer (EDS), so the corresponding EDS maps were also obtained.

3 Results and discussion

3.1 Macrographs

The welded joint was mainly composed of WZ, HAZ and BM. Figure 5 shows a macrograph of the weld cross section obtained from the two welding processes. Compared with the GTA-welded joint, the HAZ width of the U-GTPA-welded joint was smaller. However, the upper surface width of the U-GTPA WZ was smaller and the width of the lower surface was greater, which also caused an increase in the WZ depth-to-width ratio of the U-GTPA-welded joint. In addition, the two WZs contained columnar grain zones (CGZs) and equiaxed grain zones (EGZs). In the U-GTPA WZ, the area of the EGZ was larger, whereas in GTA WZ, the CGZ area was larger.

The shape, size and volume of the weld pool influence joint morphology, whereas the formation of the weld pool mainly depends on the welding heat and force. During welding, the arc pressure is directly proportional to the square of the welding current and inversely proportional to the arc radius [23]. All welding parameters in both welding tests are the same; however, U-GTPA was clearly compressed, such that an increase in the arc pressure was the main reason for the increase in the depth-to-width ratio of the U-GTPA-welded joint. Conversely, the shape of GTA was more divergent, and the pressure gradient from the edge to the center of the arc changed greatly; hence, it was difficult to obtain a weld with a large depth-to-width ratio. The HAZ width is an important feature for judging welding heat input. In terms of welding heat input, a slower heat diffusion rate typically gives a greater HAZ width. During U-GTPA welding, the effect of the pulsed arc and acoustic flow in the weld pool might promote diffusion of heat in the weld pool [24].

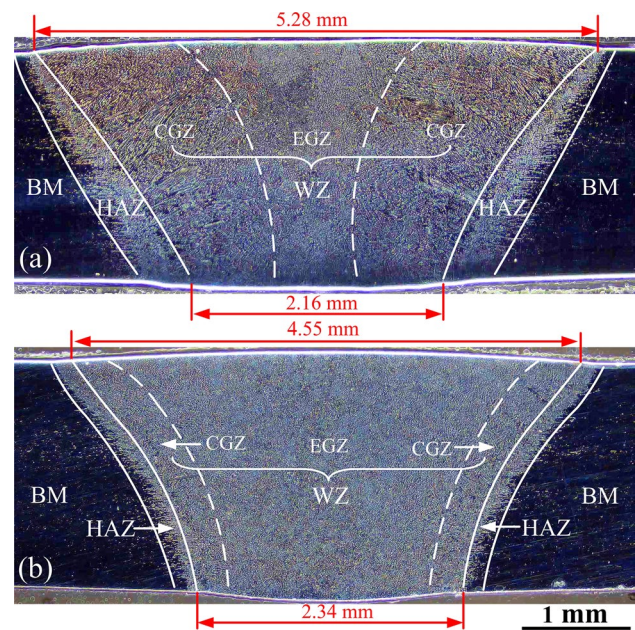


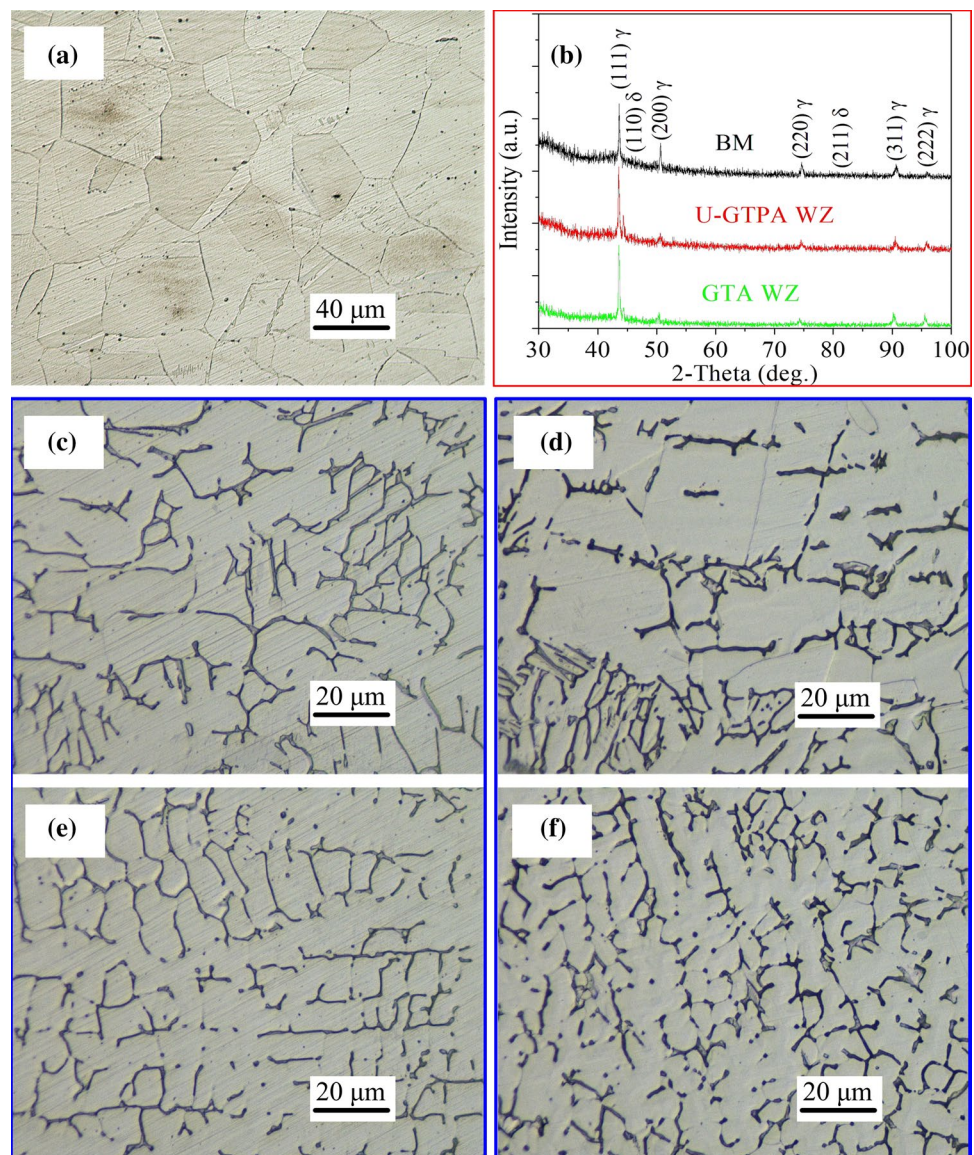
Fig. 5 Appearance of **a** GTA-welded joint and **b** U-GTPA-welded joint

3.2 Microstructure

3.2.1 Phases

The metallographic structures of the BM, WZ and HAZ in both joints were observed, XRD analysis of the BM and two WZs was performed, and these results are shown in Fig. 6. From Fig. 6a, it can be seen that microstructure of the BM of 316L stainless steel consisted of γ (fcc, white) austenite, as indicated by XRD analysis results shown in Fig. 6b. Except for the γ -austenite peak, no other peaks are found, which confirms that the BM is a single austenite structure without carbide or nitride. According to Fig. 6c–f, unlike the metallographic structure of the BM, the HAZ and WZ had δ (bcc, grey) ferrite in addition to γ -austenite. We may attribute this result to the solidification process of the weld pool, and δ -ferrite is first crystallized from the liquid. γ -austenite is formed by peritectic transformation of δ -ferrite and liquid in the initial phase. Austenite nucleates and grows around ferrite. Finally, in addition to γ -austenite obtained from peritectic transformation, residual δ -ferrite is evenly distributed in the austenite matrix, forming uneven grain boundaries [25, 26]. Compared with the GTA WZ, the δ -ferrite in U-GTPA WZ has a greater number density, which is consistent with the conclusions in Fig. 6b. This result might be attributed to the difference of the thermal cycling, such as peak temperature, duration time of the peak temperature and cooling rate, between the two welding processes. A higher peak temperature, a shorter duration time and a

Fig. 6 Microstructures in different zones: **a** BM, **c** GTA HAZ, **d** U-GTPA HAZ, **e** GTA WZ, **f** U-GTPA WZ and **b** XRD results for BM and both WZs



faster cooling rate promote the formation of the δ -ferrite structure.

3.2.2 Grain morphology

In this study, all welded joints were divided into four typical regions, i.e., BM, HAZ, CGZ and EGZ; hence, it is necessary to study the influence of the pulsed arc on the grain morphology in four typical regions. Figure 7 shows the EBSD analysis results of the four typical regions. In Fig. 7a, the BM has a typical austenitic stainless steel structure in that there are many straight grain boundaries, most of which are between 20–40 μm and the mean grain size is 37.9 μm . In addition to the angle 60° , the dislocation angle between adjacent grains had a Gaussian distribution, which indicates that there are recrystallization twins. The fraction

of the high-angle boundary (HAB) was 84.1%, including fractions of low coincidence site lattice (CSL) boundaries $\Sigma 3$ and $\Sigma 9$ of 32.0% and 0.8%, respectively. The highest intensity indicated by the red region in the polar map is only 2.977, indicating that there is a random crystallographic orientation in the BM.

Figure 7b and c shows the HAZ grain morphologies of GTA- and U-GTPA-welded joint, respectively. The grains are dominated by equiaxed grains with a random grain orientation distribution but are larger than the BM grain size. For the GTA HAZ, the mean grain size was 57.0 μm , its HAB fraction exceeded that of BM, reaching 87.7%, and the fractions of low CSL boundaries of $\Sigma 3$ and $\Sigma 9$ were 13.5% and 1.6%, respectively. The U-GTPA HAZ had a mean grain size of 39.7 μm , and the HAB fraction was only 37.7%, whereas the fractions of low CSL boundaries of $\Sigma 3$ and

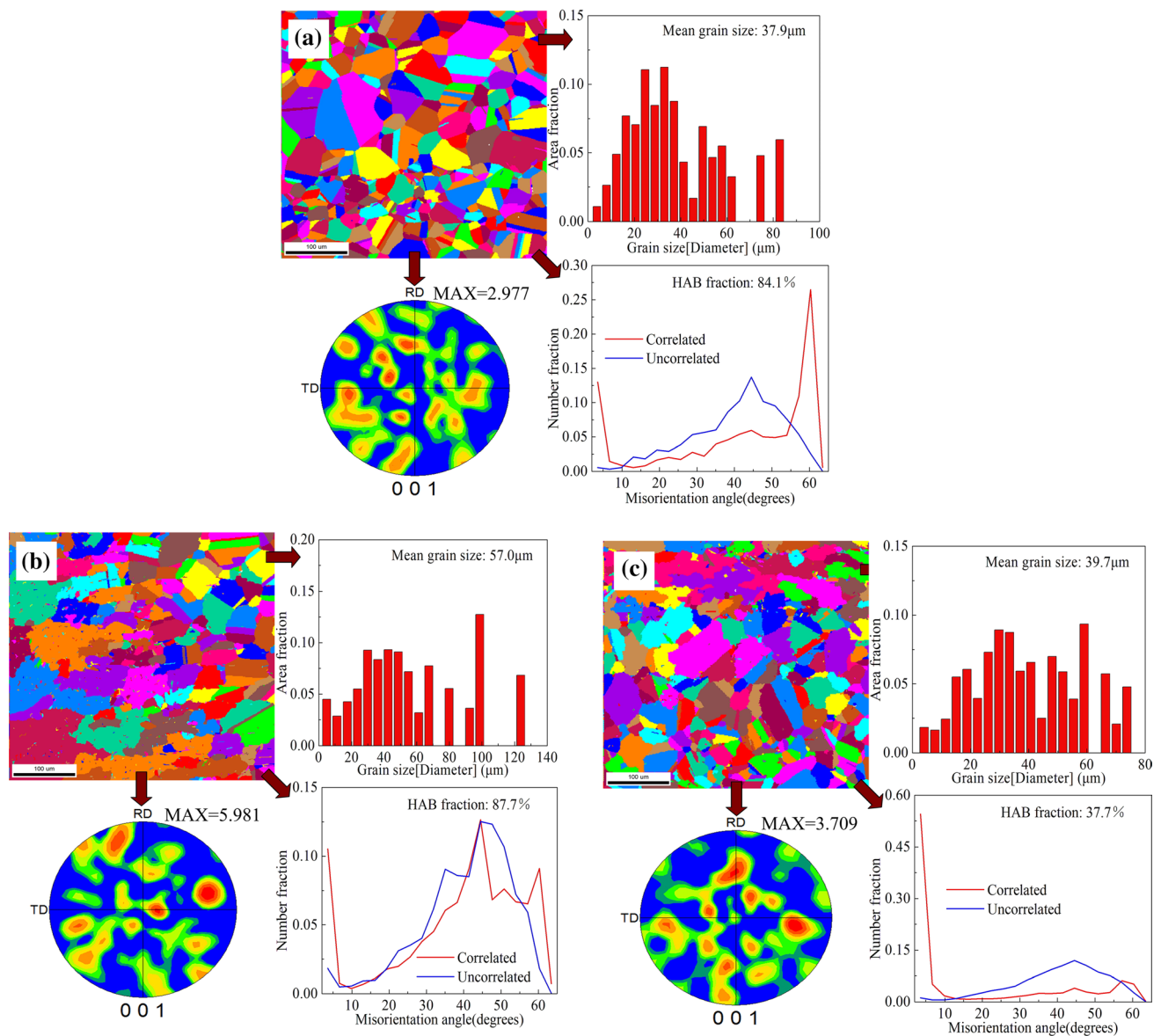


Fig. 7 EBSD analysis of four typical regions in two joints: **a** BM, **b** GTA HAZ, **c** U-GTPA HAZ, **d** GTA CGZ, **e** U-GTPA CGZ, **f** GTA EGZ and **g** U-GTPA EGZ

$\Sigma 9$ were 4.1% and 0.3%, respectively. Another difference was that twins existed in the HAZ of the GTA-welded joints but not in the HAZ of U-GTPA-welded joint. Figure 7d and e shows the grain morphologies of two CGZs, respectively. The effect of ultrasound on refining of columnar grains is not clear. The HAB fractions in CGZ of the GTA- and U-GTPA-welded joints were 71.9% and 80.1%, respectively, and no double CSL boundaries were found. The columnar grain structure showed a clear crystallographic orientation. Compared with GTA HAZ, the intensity of U-GTPA CGZ was 16.254, which indicates that a more obvious texture was formed during rapid solidification. Figure 7f and g shows the color grain and grain boundary diagrams taken from the

two EGZs, respectively. The grains were mainly randomly distributed in two EGZs. For the EGZ of the GTA-welded joint, the mean grain size was 92.1 μm and the HAB fraction was 75.9%. For the EGZ of the U-GTPA-welded joint, the mean grain size was only 56.2 μm , and the HAB fraction decreased to be 48.3%. Similarly, there were no double CSL boundaries in either joint.

For the U-GTPA-welded joint, the increase in the EGZ area as shown in Fig. 5 and the acquisition of the finer grain in the EGZ can be attributed to the following three points. First, the existence of a periodic up and down beating plasma in the center of the arc should play an important role in increasing the supercooling of the weld pool. For example,

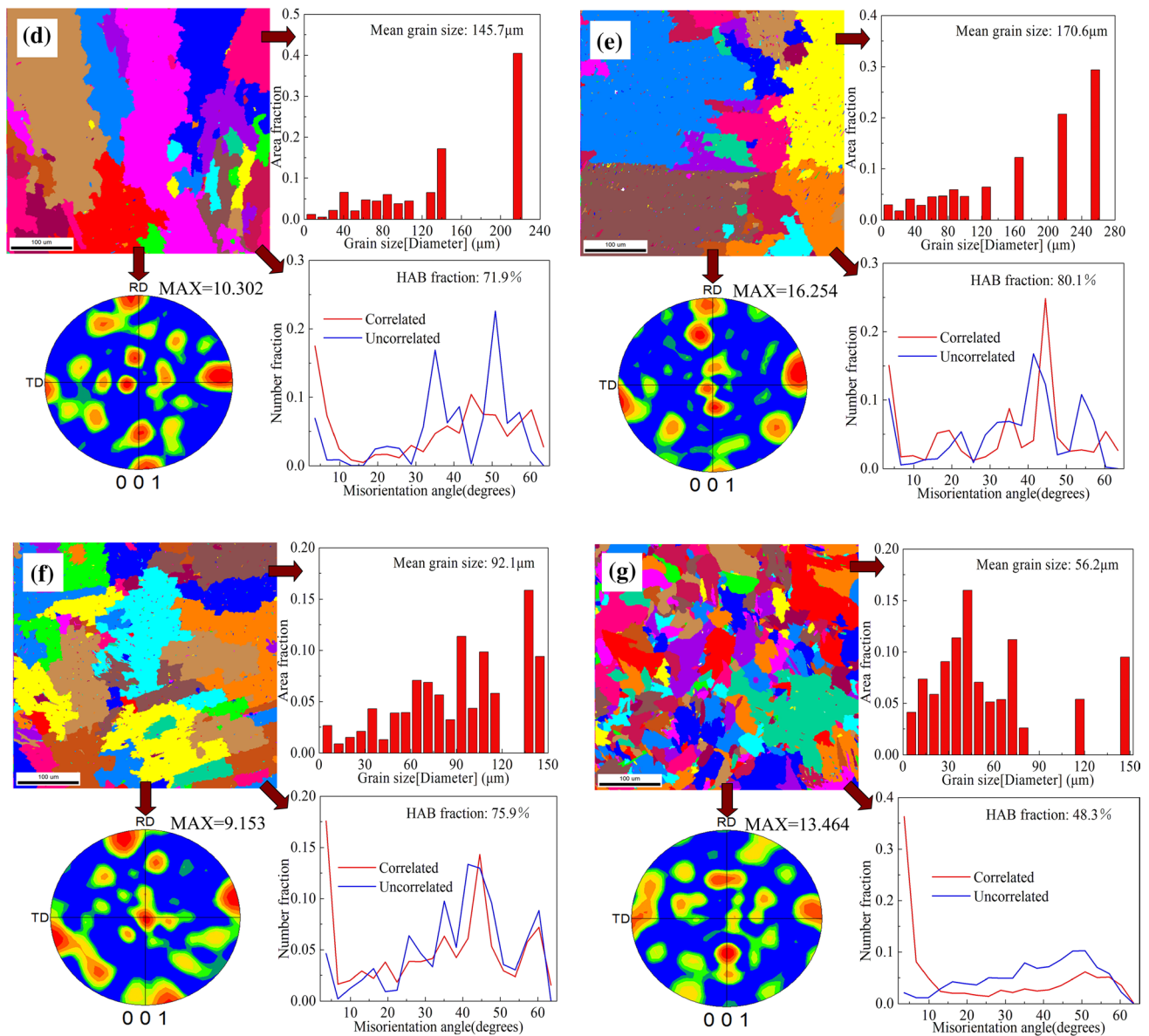


Fig. 7 (continued)

the increased constitutional supercooling during the solidification of weld pool can help dendrite fragments survive and grow into fine equiaxed grains [27]. Second, energy and phase fluctuation are two necessary conditions for nucleation. Ultrasonic vibration may accelerate the thermal movement of atoms and phase fluctuation in the weld pool, resulting in a higher number of embryos and a higher nucleation rate in the U-GTPA weld pool than those in the GTA weld pool. In other words, with the increasing local supercooling degree, the driving force of phase transformation increases. It is increasingly beneficial to reduce both the size and energy of critical nucleation, and finally the nucleation rate increases [28]. Third, additional nuclei might be produced owing to the excitation force, such as from acoustic

streaming [29] and/or acoustic cavitation [30], which breaks the growth of dendrite grains, reduces the growth rate of grains and increases the number of nuclei.

3.3 Mechanical properties

3.3.1 Microhardness profile

The variation of the microstructure inevitably leads to changes of the related mechanical properties, in which microhardness is an important index to measure weldability. Figure 8 shows the hardness variations in different zones of two welded joints obtained by two welding processes. The figure shows that the average hardness of BM was the

lowest, 172.9 HV_{0.3}, whereas that of WZ was the highest. The average hardness of WZ in the GTA-welded joint was 211.8 HV_{0.3}, whereas that in the U-GTPA-welded joint was 227.2 HV_{0.3}. Generally, the hardness of materials is affected by factors such as microstructure, phase and grain size. The hardness of the austenite was similar to that of the ferrite [31]. And no special particles affecting the hardness distribution were found in both WZs. Therefore, the increase in EGZ area and the decrease in the equiaxed grain size are the main reasons for the increase in the hardness value in the WZ of U-GTPA-welded joint compared with the WZ of GTA-welded joint without applying ultrasonic. This can be clearly observed from Figs. 5 and 7, respectively. The effect of grain size on the hardness of 316L stainless steel WZ can be proved by the use of the Hall–Petch equation. Its yield stress (σ_0) is related to the average diameter of grains (D) through the Hall–Petch equation [32]:

$$\sigma_0 = \sigma_i + \frac{K}{\sqrt{D}} \tag{1}$$

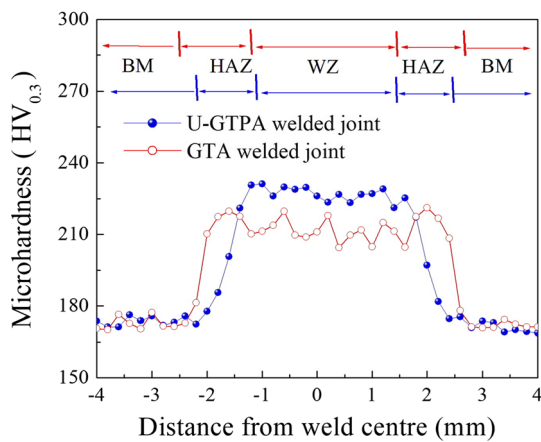


Fig. 8 Microhardness in different zones for both joints

where σ_i is the friction stress against dislocation movement, and K is a positive constant which defines the degree of dislocation accumulation behind grain boundaries. This relationship serves to demonstrate that yield stress and hardness value have opposite relation with grain size in 316L stainless steel WZ. In comparing the hardness variation of the two HAZs, the HAZ hardness variation of the GTA-welded joint was very rapid, while the HAZ hardness transition of the U-GTPA-welded joint is gentler, the possible reason is that there are more twins in the HAZ of the GTA-welded joint.

3.3.2 Tensile properties

Tensile testing is a widely used material performance evaluation test. For the BM and two welded joints studied in this paper, the tensile fracture position and tensile test results are shown in Fig. 9. The fracture positions of BM all occurred in the parallel section of the specimen. The ultimate tensile strength (UTS) of BM was 630.7 MPa, the yield strength was 353.1 MPa, and the elongation was 62.7%. The GTA-welded joint broke at the WZ. The yield strength of the GTA-welded joint was 368.0 MPa, the UTS was 584.2 MPa, and the elongation reached 40.1%. The U-GTPA-welded joint broke at the HAZ. The yield strength of the U-GTPA-welded joint was 360.4 MPa, the UTS was 625.6 MPa, and the elongation reached 50.6%. Compared with the GTA-welded joint, the UTS and elongation of the U-GTPA-welded joint were 7.1% and 26.2% greater, respectively.

To further study the mode of tensile fracture, the tensile fracture was observed by SEM, as shown in Fig. 10. Although the fracture positions were different, the fracture surfaces had a large number of equiaxed dimples formed by growth and aggregation of microporous nuclei. The dimples were different in terms of size and depth, and the fracture surfaces showed fracture morphology characteristics of ductile fracture. Figure 10a shows the fracture morphology of

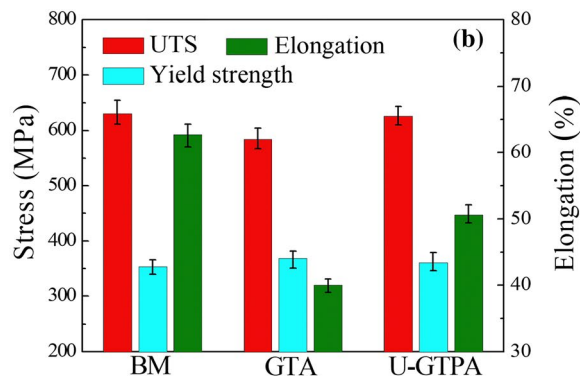
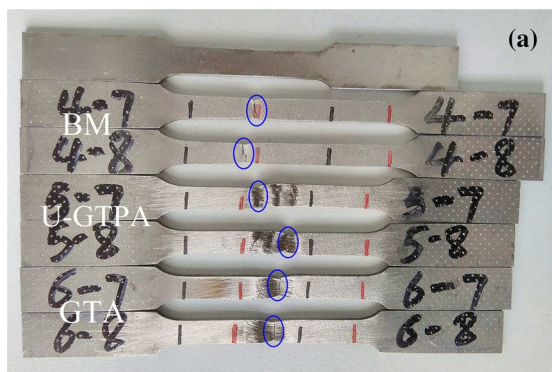


Fig. 9 a Location of tensile fracture, b tensile test results

BM. Of the three samples, the dimple depth was the largest in the BM sample and a large number of slips occurred, which correspond to the maximum UTS and elongation. Figure 10b shows the fracture morphology of the GTA-welded joint, which was broken in WZ. Among the three samples, its dimple depth was the smallest, and there was a clear tearing edge, corresponding to the minimum UTS and elongation, and the maximum yield strength. Figure 10c shows the fracture morphology of the U-GTPA-welded joint. Compared with the fracture morphology of the GTA-welded

joint, the U-GTPA-welded joint broke in the HAZ on the side close to the BM, with a larger fracture dimple depth and tensile properties similar to BM.

In the tensile deformation structure, the orientational difference between adjacent grains affects the deformation and fracture behavior to a certain extent. A larger orientation difference gives greater interface energy; hence, a large number of HABs can effectively prevent crack growth. On the other hand, the grain boundaries have high energy due to the disorders that exist in them. So, mobile dislocations

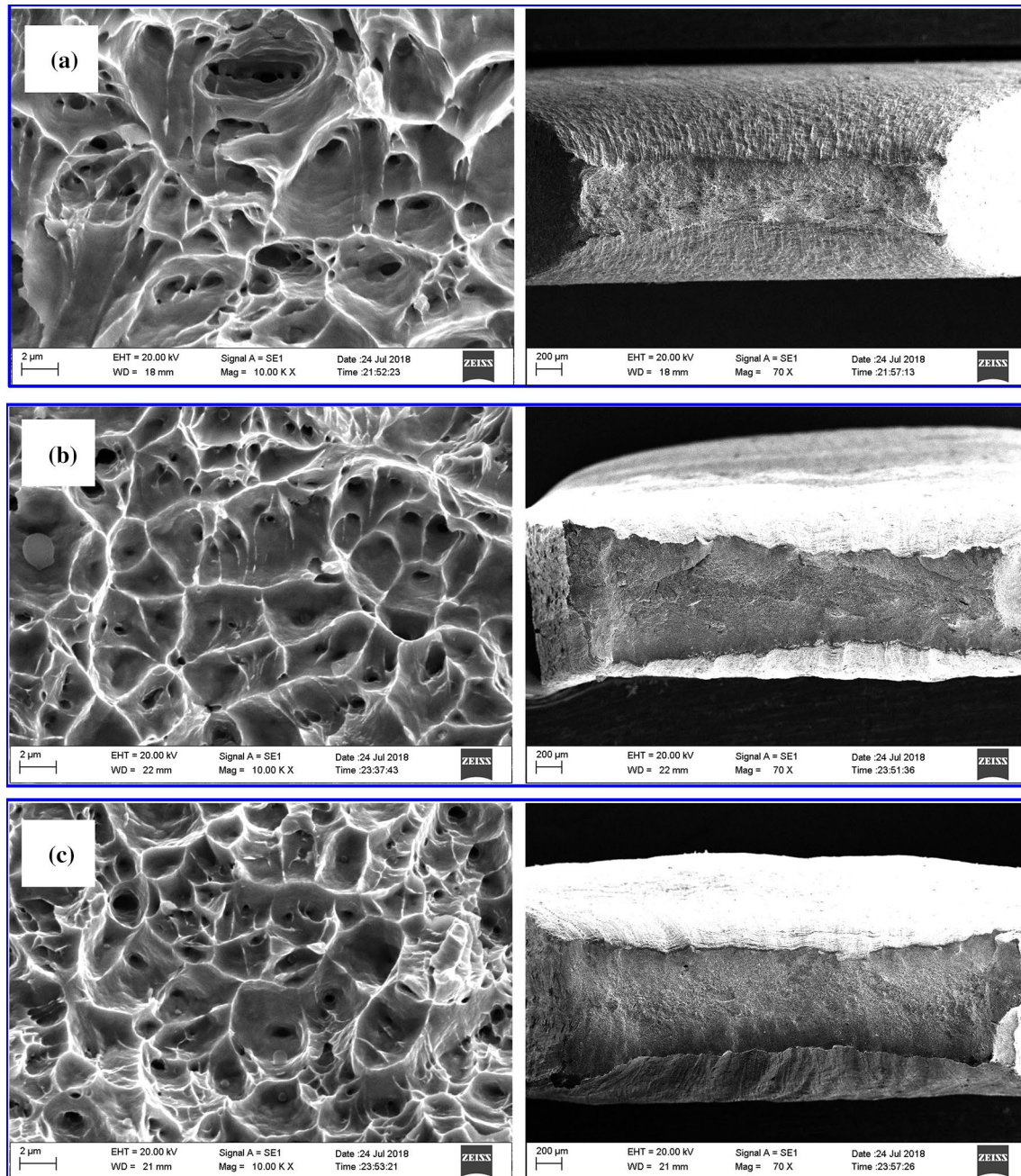


Fig. 10 SEM of tensile fracture a BM, b GTA-welded joint, c U-GTPA-welded joint

require a lot of energy to cross these grain boundaries. This results in increasing the dislocation density behind the grain boundaries and finally increasing the strength [33]. Conversely, a higher proportion of low-angle boundaries (LABs) make it easier for the dislocation to pass through. The above analysis is consistent with the experimental results in that the fracture locations of the two welded joints are located in a region with a relatively small HAB fraction in each joint. For the reason that the tensile properties of U-GTPA-welded joints are improved, in addition to fine grain strengthening, which can be explained by Hall–Petch equation (Eq. (1)), the higher δ -ferrite content also helps to improve the tensile properties, because a certain amount of intergranular δ -ferrite may prevent the formation of solidification cracks [34].

3.4 Corrosion behavior

Figure 11 shows the test results of potentiodynamic polarization curve of the WZ in two joints and BM in 3.5 wt% NaCl solution. As the electric potential increased, the passivation zones of the three samples were not obvious and the pitting stage was entered quickly. In addition, a wave peak of metastable pitting current was found in the polarization curve of the WZ of the GTA-welded joint, which represents the occurrence of a metastable hole, which might be caused by defects of the sample itself. Under the same experimental conditions, no fluctuations of metastable pitting current were found in the polarization curves of BM and the WZ of the U-GTPA-welded joints. The defects of materials, for example grain boundary inclusions, are important factors that promote metastable nucleation. For the potentiodynamic polarization curve of each sample, the corrosion potential (E_{corr}) and corrosion current density (I_{corr}) were determined by Tafel extrapolation. The means of the three E_{corr} and I_{corr} values obtained are listed in Table 2.

As shown in Table 2, the maximum value of I_{corr} ($20.61 \times 10^{-7} \text{ A/cm}^2$) occurs in the WZ of the GTA-welded joint and the minimum value ($10.60 \times 10^{-7} \text{ A/cm}^2$) in BM. The corrosion rate increases as the corrosion current density increases; hence, the WZ corrosion rate of the GTA-welded joint is fastest, whereas the BM corrosion rate is slowest. In the WZ of the U-GTPA-welded joint, E_{corr} achieves a maximum value ($0.09 \text{ V}_{\text{SCE}}$), whereas in the WZ of the GTA-welded joint, E_{corr} obtains the minimum value ($0.03 \text{ V}_{\text{SCE}}$). As the corrosion potential decreased, the corrosion sensitivity or corrosion tendency increased. That is to say, in 3.5% NaCl solution, the corrosion tendency of the WZ of the U-GTPA-welded joint and the BM and WZ of the GTA-welded joint increase successively.

SEM images of the two WZs and the EDS element mappings after potentiostatic polarization experiment are shown in Fig. 12. Under the same experimental conditions, the WZ corrosion of the GTA-welded joint was more serious. A large corrosion pit formed in the WZ of GTA is shown in Fig. 12a.

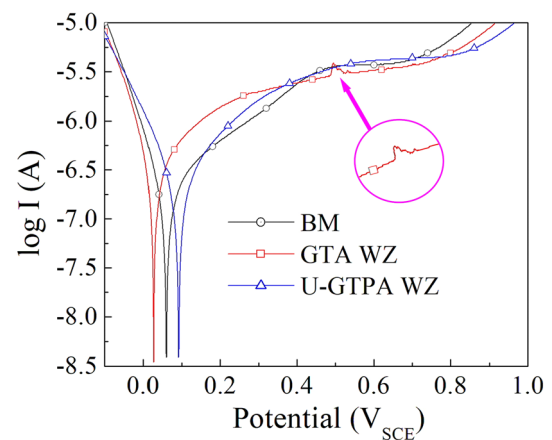


Fig. 11 Tafel polarization curves of the BM and both WZs

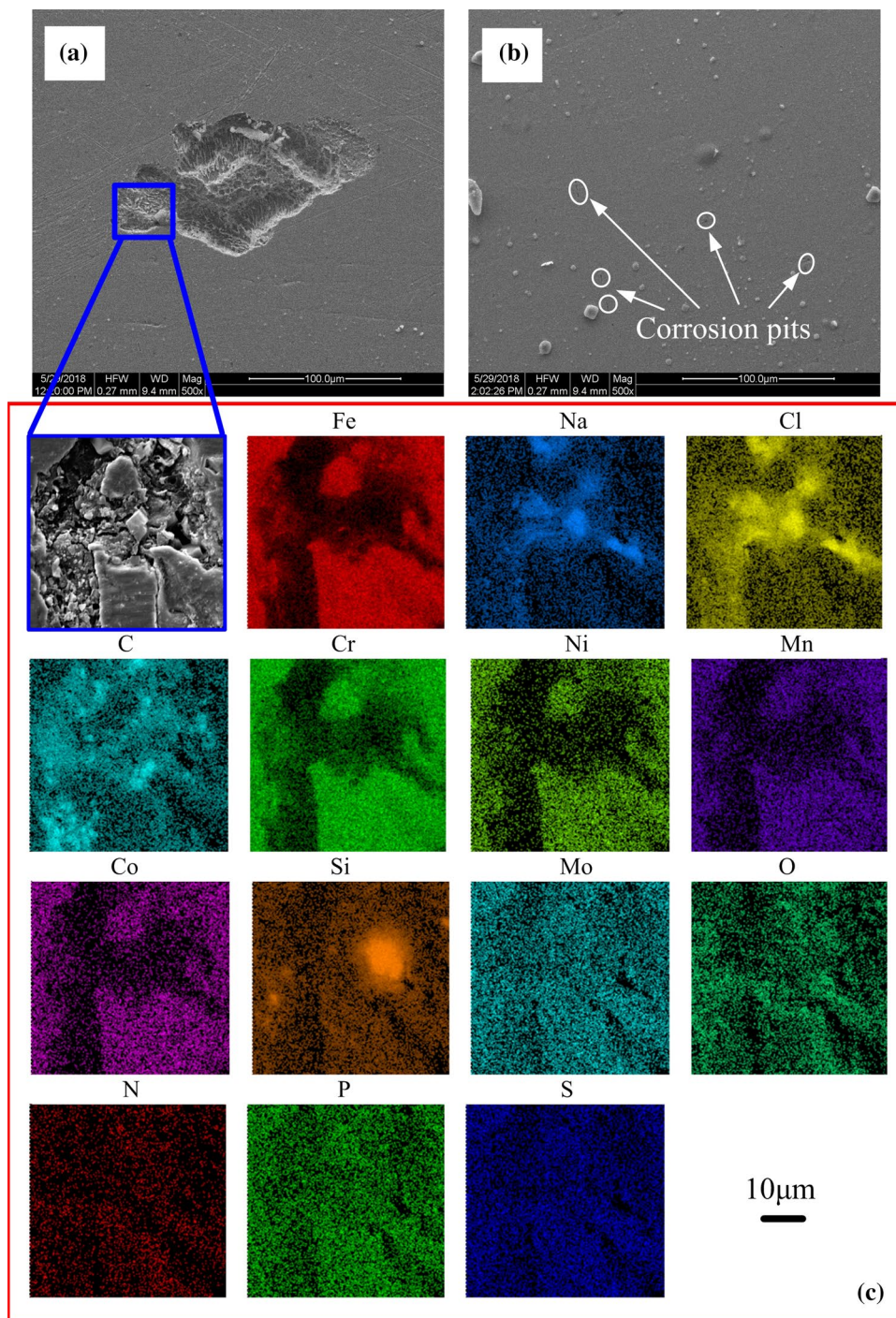
Table 2 Electrochemical analysis results from Tafel curves in Fig. 11

| | BM | GTA WZ | U-GTPA WZ |
|---|------------------------|------------------------|------------------------|
| $I_{\text{corr}} (\text{A/cm}^2)$ | 10.60×10^{-7} | 20.61×10^{-7} | 13.45×10^{-7} |
| $E_{\text{corr}} (\text{V}_{\text{SCE}})$ | 0.06 | 0.03 | 0.09 |

Conversely, only a few small corrosion pits or holes were found in the WZ of the U-GTPA-welded joint, as shown in Fig. 12b, indicating good corrosion resistance. The EDS element mapping analysis at the edge of the corrosion pit of the WZ in the GTA-welded joint is shown in Fig. 12c. The loss of the elements Fe, Cr, Ni, Mn and Co was most serious in the corroded zone, whereas accumulation of C was most obvious.

The microstructure variation of the WZ in the welded joint directly changes the material corrosion resistance. Wasnik et al. [35] confirmed that elements C, Fe and Cr contained in austenite can form complex carbides $[(\text{Cr}, \text{Fe})_{23}\text{C}_6]$, which tend to form supersaturated solid solutions during rapid cooling. However, on slow cooling, to maintain the heat balance, carbides will precipitate from the solid solution and distribute at the grain boundary. Bennett et al. [36] reported that high-energy grain boundaries are favorable for obtaining a high carbide nucleation rate and high diffusion rate. That is to say, a higher HAB fraction will promote formation of carbides and accelerate the loss of Cr in the grain boundary. Sahlaoui et al. [37] posited that precipitation of carbides along grain boundaries results in a Cr deficiency near the grain boundary, which causes more micro-cells with small anodes or large cathodes to form near grain boundaries and accelerates corrosion in that region. For the U-GTPA welding process, the cooling rate of the weld pool should be faster, which is not conducive to carbide precipitation, and a higher proportion of LAB in the WZ is also not conducive to improving the carbide nucleation rate and diffusion rate.

Fig. 12 Corrosion morphologies after potentiodynamic tests of **a** GTA WZ and **b** U-GTPA WZ, **c** EDS element mapping analysis of the corrosion pit in the GTA WZ



In addition, in the WZ, higher ferrite content is associated with higher Cr content, which also alleviates the formation of Cr poor regions [38, 39]. The combination of these factors makes the corrosion resistance of the U-GTPA WZ better than that of the GTA WZ. The five elements Ni, Co, Fe, Cr and Mn are in the same period and have similar atomic radii and slightly varying electrode potentials ($Ni > Co > Fe > Cr > Mn$), which might explain why these elements are more prone to loss in the corroded zone.

4 Conclusions

The microstructure, mechanical properties and corrosion behavior of 316L stainless steel-welded joints obtained by GTA and U-GTPA welding processes were systematically studied, and the main conclusions drawn are as follows:

- (1) U-GTPA exhibits a significant influence on the morphology of welded joint. Under this combined influ-

ence of the increased arc pressure and heat dissipation rate, compared with the GTA-welded joint, the HAZ width of the U-GTPA-welded joint was smaller, the WZ depth-to-width ratio was greater.

(2) For the U-GTPA-welded joint, the presence of the pulsed arc, ultrasonic vibration, and excitation force could help refine the grains. In HAZ, the mean grain size was 39.7 μm and the HAB fraction was only 37.7%. In EGZ, the mean grain size was 56.2 μm and the HAB fraction decreased to 48.3%.

(3) The increase in EGZ area and the decrease in the equiaxed grain size were the main reasons for the increase in the strength and hardness. Compared with the GTA-welded joint, the UTS and elongation of the U-GTPA-welded joint increased by 7.1% and 26.2%, respectively.

(4) According to this difference for both welded joints at the fracture position in the tensile testing, it shows that a small amount of HABs were not beneficial in improving joint tensile properties. However, the lower HAB fraction and higher ferrite content in U-GTPA WZ slowed the loss of Cr in the grain boundary, resulting in a good corrosion resistance in 3.5% NaCl solution.

Acknowledgments This work was supported by the National Natural Science Foundation of China (No. 51705072), the Science Foundation for the Excellent Youth Scholars of the Science and Technology Department of Jilin Province (No. 20190103037JH), China, the Research Program on Science and Technology of the 13th Five-Year Plan of the Education Department of Jilin Province (No. JJKH20180428KJ), China and the Chinese Government Scholarship from China Scholarship Council (No. 201807790001).

Compliance with ethical standards

Conflict of interest The authors declare that they have no conflict of interest.

Ethical statement This paper is an original work and has been neither published nor submitted for publication elsewhere.

References

- Kang JH, Noh HS, Kim KM, Lee SC, Kim SJ. Modified Ni equivalent for evaluating hydrogen susceptibility of Cr–Ni based austenitic stainless steels. *J Alloy Compd.* 2017;696:869–74.
- Babu KA, Mandal S, Athreya CN, Shakthipriya B, Sarma VS. Hot deformation characteristics and processing map of a phosphorous modified super austenitic stainless steel. *Mater Des.* 2017;115:262–75.
- Xi T, Shahzad MB, Xu D, Zhao J, Yang C, Qi M, Yang K. Copper precipitation behavior and mechanical properties of Cu-bearing 316L austenitic stainless steel: a comprehensive cross-correlation study. *Mater Sci Eng A-Struct.* 2016;675:243–52.
- Sun H, Sun Y, Zhang R, Wang M, Tang R, Zhou Z. Study on hot workability and optimization of process parameters of a modified 310 austenitic stainless steel using processing maps. *Mater Des.* 2015;67:165–72.
- Lundberg M, Saarimäki J, Moverare JJ, Calmunger M. Surface integrity and fatigue behaviour of electric discharged machined and milled austenitic stainless steel. *Mater Charact.* 2017;124:215–22.
- Mankari K, Acharyya SG. Failure analysis of AISI 321 stainless steel welded pipes in solar thermal power plants. *Eng Fail Anal.* 2018;86:33–43.
- Hua Z, Zhu S, An B, Iijima T, Gu C, Zheng J. The finding of hydrogen trapping at phase boundary in austenitic stainless steel by scanning Kelvin probe force microscopy. *Scripta Mater.* 2019;162:219–22.
- Yamaguchi T, Hagino H. Formation of a titanium–carbide–dispersed hard coating on austenitic stainless steel by laser alloying with a light-transmitting resin. *Vacuum.* 2018;155:23–8.
- Xin J, Song Y, Fang C, Wei J, Huang C, Wang S. Evaluation of inter-granular corrosion susceptibility in 316LN austenitic stainless steel weldments. *Fusion Eng Des.* 2018;133:70–6.
- Gao Z, Jiang P, Wang C, Shao X, Pang S, Zhou Q, Li X, Wang Y. Study on droplet transfer and weld quality in laser–MIG hybrid welding of 316L stainless steel. *Int J Adv Manuf Tech.* 2017;88:483–93.
- Feng Y, Luo Z, Liu Z, Li Y, Luo Y, Huang Y. Keyhole gas tungsten arc welding of AISI 316L stainless steel. *Mater Des.* 2015;85:24–31.
- Garcia C, de Tiedra MP, Blanco Y, Martin O, Martin F. Intergranular corrosion of welded joints of austenitic stainless steels studied by using an electrochemical minicell. *Corros Sci.* 2008;50:2390–7.
- Tseng KH, Hsu CY. Performance of activated TIG process in austenitic stainless steel welds. *J Mater Process Technol.* 2011;211:503–12.
- Sabzi M, Dezfuli SM. Drastic improvement in mechanical properties and weldability of 316L stainless steel weld joints by using electromagnetic vibration during GTAW process. *J Manuf Process.* 2018;33:74–85.
- Thangapandian N, Prabu SB, Padmanabhan KA. Effects of die profile on grain refinement in Al–Mg alloy processed by repetitive corrugation and straightening. *Mater Sci Eng A Struct.* 2016;649:229–38.
- Xie RS, Chen XG, Lai ZW, Liu L, Zou GS, Yan JC, Wang WX. Microstructure, mechanical properties and mechanism of ultrasound-assisted rapid transient liquid phase bonding of magnesium alloy in air. *Mater Des.* 2016;91:19–27.
- Xie W, Huang T, Yang C, Lin S, W, Xu, Comparison of microstructure, mechanical properties, and corrosion behavior of Gas Metal Arc (GMA) and Ultrasonic-wave-assisted GMA (U-GMA) welded joints of Al–Zn–Mg alloy. *J Mater Process Technol.* 2020;277:116470.
- Han Q. Ultrasonic processing of materials. *Metall Mater Trans B.* 2015;46:1603–14.
- Sun QJ, Lin SB, Yang CL, Zhao GQ. Penetration increase of AISI 304 using ultrasonic assisted tungsten inert welding. *Sci Technol Weld Joi.* 2009;14:765–7.
- Xie WF, Fan CL, Yang CL, Lin SB. Effect of acoustic field parameters on arc acoustic binding during ultrasonic wave-assisted arc welding. *Ultrason Sonochem.* 2016;29:476–84.
- Xie W, Fan C, Yang C, Lin S, Zhang Y. Characteristics of acoustic-controlled arc in ultrasonic wave-assisted arc. *Acta. Phys. Sin.* 2015;64:095201.
- Chinese standard GB/T 228.1–2010. *Metallic materials–Tensile testing at ambient temperature (in Chinese)*, 2010.

23. Chen S, Yan Z, Jiang F, Lu Z. The pressure distribution of hollow cathode centered negative pressure arc. *J Manuf Process*. 2016;23:21–8.
24. Zhao J, Wu S, Wan L, Chen Q, An P. Evolution of microstructure of semisolid metal slurry in ultrasound field. *Acta Metall Sin*. 2009;45:314–9.
25. Chen X, Li J, Cheng X, Wang H, Huang Z. Effect of heat treatment on microstructure, mechanical and corrosion properties of austenitic stainless steel 316L using arc additive manufacturing. *Mater Sci Eng A-Struct*. 2018;715:307–14.
26. Liu K, Li Y, Wang J. Microstructure and low-temperature mechanical properties of 304 stainless steel joints by PAW+ GTAW combined welding. *J Mater Eng Perform*. 2016;25:4561–73.
27. Yuan T, Luo Z, Kou S. Mechanism of grain refining in AZ91 Mg welds by arc oscillation. *Sci Technol Weld Joi*. 2017;22:97–103.
28. Mao G, Cao R, Chen J, Guo X, Jiang Y. Analytical investigation of grain size dependence of microhardness in high nickel-containing reheated weld metal. *Arch Civ Mech Eng*. 2017;17:935–42.
29. Wang G, Croaker P, Dargusch M, McGuckin D, StJohn D. Simulation of convective flow and thermal conditions during ultrasonic treatment of an Al–2Cu alloy. *Comput Mater Sci*. 2017;134:116–25.
30. Feng X, Zhao F, Jia H, Li Y, Yang Y. Numerical simulation of non-dendritic structure formation in Mg–Al alloy solidified with ultrasonic field. *Ultrason Sonochem*. 2018;40:113–9.
31. Zhao Y, Wang Y, Tang S, Zhang W, Liu Z. Edge cracking prevention in 2507 super duplex stainless steel by twin-roll strip casting and its microstructure and properties. *J Mater Process Technol*. 2019;266:246–54.
32. Liu T, Li Y, Ren Y. Effect of Pr inoculation and crystal size on the hall–petch relationship for Al–30 wt%Mg₂Si composites. *Mater Lett*. 2018;214:6–9.
33. Immanuel RJ, Panigrahi SK, Racineux G, Marya S. Investigation on crashworthiness of ultrafine grained A356 sheets and validation of hall–petch relationship at high strain–rate deformation. *Mater Sci Eng A Struct*. 2017;701:226–36.
34. Kurzynowski T, Gruber K, Stopyra W, Kuźnicka B, Chlebus E. Correlation between process parameters, microstructure and properties of 316L stainless steel processed by selective laser melting. *Mater Sci Eng A-Struct*. 2018;718:64–73.
35. Wasnik DN, Dey GK, Kain V, Samajdar I. Precipitation stages in a 316L austenitic stainless steel. *Scripta Mater*. 2003;49:135–41.
36. Bennett BW, Pickering HW. Effect of grain boundary structure on sensitization and corrosion of stainless steel. *Metall Trans A*. 1991;18:1117–24.
37. Sahlaoui H, Makhlof K, Sidhom H, Philibert J. Effects of ageing conditions on the precipitates evolution, chromium depletion and intergranular corrosion susceptibility of AISI 316L: experimental and modeling results. *Mater Sci Eng A-Struct*. 2004;372:98–108.
38. Liu S, Liu Z, Wang Y, Tang J. A comparative study on the high temperature corrosion of TP347H stainless steel, C22 alloy and laser-cladding C22 coating in molten chloride salts. *Corros Sci*. 2014;83:396–408.
39. Wang J, Su H, Chen K, Du D, Zhang L, Shen Z. Effect of δ -ferrite on the stress corrosion cracking behavior of 321 stainless steel. *Corros Sci*. 2019;158:108079.

Publisher's Note Springer Nature remains neutral with regard to jurisdictional claims in published maps and institutional affiliations.